Composite Structures 293 (2022) 115751

Contents lists available at ScienceDirect

Composite Structures

journal homepage: www.elsevier.com/locate/compstruct

Assessing stiffness degradation of stiffened composite panels in post-buckling compression-compression fatigue using guided waves

Nan Yue [a,d,*], Agnes Broer [a,d], William Briand [b], Marc Rébillat [b], Theodoros Loutas [c], Dimitrios Zarouchas [a,d]

[a] Structural Integrity and Composites Group, Faculty of Aerospace Engineering, Delft University of Technology, Delft, The Netherlands
[b] PIMM, Arts et Metiers Institute of Technology, CNRS, Cnam, HESAM University, Paris, France
[c] Applied Mechanics Laboratory, Department of Mechanical Engineering and Aeronautics, University of Patras, 26504 Rio, Greece
[d] Center of Excellence in Artificial Intelligence for Structures, Prognostics & Health Management, Aerospace Engineering Faculty, Delft University of Technology, The Netherlands

ARTICLE INFO

Keywords:
CFRP
Stiffened panel
Stiffness degradation
Compression-compression fatigue
Guided waves
Structural health monitoring

ABSTRACT

The application of structural health monitoring (SHM) in composite airframe structural elements under long-term realistic fatigue loading needs to consider the structural behavior on the global level, which is an intricate task. The overall structural stiffness is a key design parameter for composite structures and the stiffness degradation under fatigue loading is closely related to the damage accumulation and failure mechanism which can be used as an indicator for the structural degradation. Therefore, this paper investigates the use of guided waves in axial stiffness degradation estimation for stiffened carbon fiber reinforced polymer (CFRP) composite panels under post-buckling compression-compression (C-C) fatigue loads. Impacted or artificially debonded stiffened composite panels are tested under fatigue until failure and guided waves are acquired using a network of piezoelectric (PZT) sensors at fixed cycle intervals. The guided wave phase velocity along the loading direction is extracted to estimate the axial stiffness degradation with the consideration of mode conversion and failure of PZT sensors. The estimated stiffness of five stiffened composite panels matches well with the stiffness calculated from the load–displacement curves. The estimated stiffness is also assessed using prognostic performance metrics and shows good potential for being used as a health indicator for prognostic purposes.

1. Introduction

Fibre reinforced polymer composite materials have been favoured by multiple industries, especially the aerospace industry, in pursue of high structural performance with low weight due to its superior specific stiffness and strength, as well as its flexibility, which enables tailored design for specific applications. However, the lack of understanding in the complicated damage and failure mechanisms of composite materials under long term use has led to the overdesign (i.e., high safety factor) of the composite structures to mitigate the risk of catastrophic failure, which diminishes the advantages of weight reduction.

Fatigue degradation in composite structures is not only a material phenomenon but also a structural phenomenon, which is determined by the material characteristics and the geometry of the structure. Different to the localised damage growth in metals, fatigue damage in composites occurs more globally [1]. The damage mechanics of composite laminates under fatigue loading is complex because of the continuous stress redistribution caused by the non-homogeneous and multi-interface nature of composite laminates, as well as the presence of manufacturing defects [1–3]. In tension–tension (T-T) fatigue, the main damage mechanisms are matrix cracking, delamination, and fibre breakage. The damage evolution process can be characterised into three stages, each stage with a dominant damage mechanism [4]. The first stage is dominated by the accumulation of matrix cracks in the off-axis plies until the crack density saturates, followed by the second stage where delamination grows from the tips of the matrix cracks. The third and the last stage primarily sees the breakage of fibres in on-axis plies. However, the damage accumulation mechanism in C-C fatigue is different from that in T-T fatigue [5]. Liu et al. [6] investigated the damage mechanism in T-T and C-C fatigue of CFRP specimens with presence of matrix voids. The

* Corresponding author at: Nan Yue, Structural Integrity and Composites Group, Faculty of Aerospace Engineering, Delft University of Technology, Kluyverweg 1, 2629 HS Delft, The Netherlands.
E-mail address: N.Yue@tudelft.nl (N. Yue).

https://doi.org/10.1016/j.compstruct.2022.115751
Received 12 October 2021; Received in revised form 14 March 2022; Accepted 8 May 2022
Available online 13 May 2022

voids accelerate the matrix crack initiation and accumulation in T-T fatigue, whiles it stimulates fibre–matrix interface failure and delamination in C-C fatigue, leading to earlier unstable fibre fracture and shorter fatigue life.

Another key weakness of composite laminates is its vulnerability to impact, which can cause a mixture of matrix cracks, delaminations, as well as fibre breakage. The strength, especially the compressive strength, of the composite structure can be significantly compromised by the impact damage [7–9]. While being detrimental to the structural integrity, the impact damage can often be barely noticeable on the surface in visual inspections [10].

To ensure structural integrity and safety, non-destructive evaluation (NDE) methods have been developed and are widely used in the aeronautical industry. The use of NDE methods is accomplished with scheduled maintenance, where an aircraft is taken out of service after a certain number of flight hours for inspection and necessary repair or replacement. However, the out-of-service inspection contributes to a large fraction of the maintenance time and cost but is not always required based on the aircraft's structural state. In the last few decades, structural health monitoring (SHM) has received increasing attention from both academia and industry. The main difference of SHM methods from NDE methods is that the former utilizes permanently installed sensors to monitor autonomously, i.e. without any human intervention, the structural integrity. Combined with on-board data acquisition and other complimentary systems, SHM has the potential of online inspection, which opens the door to condition-based maintenance (CBM). In contrast to scheduled maintenance incorporated with NDE, CBM powered by SHM is guided by the integrity of the structure rather than by a predetermined schedule. Moreover, the continuous monitoring of the structure will also enhance the understanding of the long term behaviour of the structures, which in turn promotes light-weight and energy-saving structural design.

Guided waves, such as Lamb waves, is one of the most popular SHM techniques for thin-walled structures used in the aerospace industry. Thanks to the convenient and efficient excitation of guided wave using piezoelectric (PZT) sensors, guided wave based SHM (GWSHM) has been successfully implemented for impact damage detection, localization, and sizing in real scale composite airframe structures [11–14]. Practicality issues of using GWSHM for aerospace applications with large variation in environmental and operational conditions have also been investigated and multiple reliable compensation methods have been proposed and validated [15–17].

In recent years, attention has been given to the ability of guided wave for material characterisation. Pant et al.[18,19] derived a 3D analytical solution of Lamb wave propagation in composite laminates and demonstrated the effect of material properties variability including E_{11}, E_{22}, G_{12} and density on Lamb wave dispersion relations and the slowness curve. At all frequency-thickness product ranges, S0 mode was found to be mainly sensitive to the fibre dominated properties whereas the A0 mode was found to be mainly sensitive to the matrix dominated properties. Moreover, it was found that S0 mode was sensitive to the matrix dominated properties at higher frequency-thickness product range while A0 mode was sensitive to the fibre dominated properties at lower frequency-thickness product range. Zhao et al. used genetic algorithms to estimate nine stiffness coefficients of composite laminates by measuring Lamb wave phase velocities with Laser generated ultrasounds [20]. Giannakeas et al. estimated material properties of composite laminates using a semi-analytical finite element method for the computation of dispersion curves and a genetic algorithm to derive material properties that result in the best match with experimental results [21].

The capability of guided waves in monitoring fatigue damage accumulation in composite coupons has also been investigated by several research groups. Rheinfurth et al. [5] investigated the applicability of Lamb wave in monitoring mechanically induced fatigue damage in quasi-isotropic carbon fibre reinforced polymer (CFRP) composite laminates. The correlations between crack density, stiffness degradation, and the decrease in the normalized A0 mode phase velocity were observed for T-T and tension–compression (T-C) fatigue loading. In contrast, for C-C fatigue loading, the decrease in A0 mode velocity was significantly smaller than the other two fatigue cases, which was due to the smaller number of cracks and the slight stiffness degradation in the gauge region until the failure at the unsupported area between the end tab and the anti-buckling device. Tao et al. [22] utilised S0 mode Lamb wave phase velocity at low frequency ranges to characterise fatigue damage accumulation in quasi-isotropic glass fibre reinforced polymer (GFRP) composite laminates under constant amplitude T-T fatigue load. The same research group also described the mode conversion phenomenon that can potentially be utilized for fatigue damage characterization [23]. In 2011, NASA published a database of T-T fatigue-to-failure tests of composite coupons with dogbone geometry (15.24 cm $\times$ 25.4 cm) instrumented with PZT sensors, where several Lamb wave features showed positive correlation with the crack density and delamination size observed using X-ray [24]. Based on this database, Mishra and Vanil [25] developed an approach for predicting the delamination growth and the remaining useful life of the structure using Lamb waves. The damage sensitive Lamb wave features were extracted using principal component regression and the damage growth and failure were modelled and predicted using Wiener process. Peng et al. [26] combined a mechanical stiffness degradation model and Lamb wave detected global stiffness degradation using a Bayesian inference framework for T-T fatigue life prediction.

It is evident that guided waves are capable of monitoring the change of material properties caused by fatigue damage accumulation. However, most of the aforementioned research is mainly focused on T-T fatigue loading on composite coupons. Guided wave monitoring of composite specimen in C-C fatigue has received much less attention and has not yet been fully explored. The limited study in standard coupon compression testing might be the result of the restrictions in guided wave instrumentation due to the small coupon size to prevent buckling or the use of anti-buckling device [27,28]. In contrast to T-T fatigue, C-C fatigue has a different damage evolution and failure mechanism. Worsened by damage caused by unexpected impact events, the fatigue life of composite structures can be significantly shortened. For stiffened composite structures designed to withstand compressive load, the disbond of the stiffener and skin caused by impact could be the dominant failure mechanism, which is closely related to the buckling behavior determined by the geometry of the structure [29,30].

From an engineering point of view, what matters is whether the structure can still handle what it has been designed for. However, the classical GWSHM methods focus on local approaches where local changes in material properties due to the damage occurrence are being monitored (position, severity). Here, we take the viewpoint of engineers and try to figure out, on a global scale, how all the individual and spatially distributed fatigue damage, contributes to global structural degradation that will be informative from a structural design point of view.

For composite structures, stiffness is well understood and commonly used for the design and optimization process. The decrease in stiffness under fatigue loading is closely related to the damage accumulation and failure mechanism. For complex structural geometries such as stiffened panels, the stiffness in load bearing direction can be experimentally assessed throughout the fatigue life which contains important information on the global fatigue degradation and damage accumulation and can be used as an indicator of the structural degradation for prognostic purposes. In contrast to the prognostic method developed with a health indicator without physical meaning, the prognostic method based on a physically meaningful parameter such as stiffness degradation can be more informative and allows improvement with deeper understanding of the phenomenon.

The purpose of this paper is thus to explore the capability of guided waves in assessing the long-term fatigue degradation of complex

composite structures and examine the potential of using the guided wave based stiffness estimation as health indicator for prognosis, i.e. remaining useful life prediction. In particular, the experimental effort is devoted to the rarely studied post-buckling compression-compression fatigue of CFRP structures. The fatigue degradation is assessed globally by estimating the axial stiffness using guided wave phase velocity in order to evaluate the global load bearing capacities that can be used for failure and remaining useful life prediction. The development of a guided wave-based monitoring method considers the structural degradation behaviour as well as practical issues including wave mode conversion and sensor degradation. In order to demonstrate the effectiveness of the proposed approach, CFRP composite panels with T-stiffeners are tested under post-buckling C-C fatigue loads with the presence of impact damage or an artificial disbond. The fitness of using the proposed stiffness estimation method for prognostic purposes are examined by the prognostic performance matrices and is compared to the reference stiffness measured from load-displacement data.

This paper is organised as follows. Section 2 describes the experimental set-up. Section 3 shows the post buckling behaviour and the fatigue degradation of the stiffened panels. Section 4 presents the method to estimate stiffness degradation using guided wave. Section 5 shows the results and Section 6 discusses the findings of this work and suggests future works. The paper is finally concluded in Section 7.

2. Experimental setup

A generic element of an aircraft wing structure, a single-stiffener CFRP composite panel, is considered in this work. The test campaign includes a total number of 12 nominally identical panels. Five of the stiffened panels are sensorised with PZT sensors for guided wave acquisition. The other seven stiffened panels are not sensorised with PZT sensors but were tested under the same load conditions. Within the scope of this work, only the five panels equipped with PZT sensor are analysed.

Each specimen consists of a skin panel and a co-cured T-stiffener, both made from IM7/8552 unidirectional prepreg. The dimension of the panel is shown in Fig. 1. The layup sequence of the skin and stiffener are $[45/-45/0/45/90/-45/0]_s$ and $[45/-45/0/45/-45]_s$, respectively. Two epoxy resin tabs were moulded to the ends of the panel to create flat loading surfaces during manufacturing. The surfaces of the tabs were further machined in order to achieve parallelism of less than 0.2 mm between the loading surfaces, and thereby ensure a distributed and aligned compressive load introduction into the panels.

Five specimens are sensorised with piezoelectric sensors (Noliac NCE51, 20 mm in diameter and 0.5 mm in thickness) on the stiffener side for guided wave generation and acquisition, as shown in Error! Reference source not found.. Eight sensors are surface mounted on each specimen using a two-component epoxy adhesive (Loctite EA9492). Four sensors are placed on the skin panel, two sensors are placed on top of the stiffener-skin bondline and two sensors are placed on the stiffener web.

The impact damage concerned in this work is barely visible impact damage (BVID) caused by a low-velocity impact with a surface dent barely detectable by visual inspection from a distance of 1.0 m under artificial lighting. Impact trails were performed over a range of energies, and the 10 J impact resulted in BVID and thus was selected as impact energy for the composite panels tested in fatigue. A C-scan image after a 10 J impact damage on the stiffener foot is shown in Fig. 2.

Impact is performed on four sensorised panels (C3, C4, C5, C9) prior to the fatigue test, resulting in barely visible impact damage (BVID). On panel S23, a manufacturing defect is simulated as a disbond of the stiffener foot by inserting a Teflon layer during the manufacturing of the

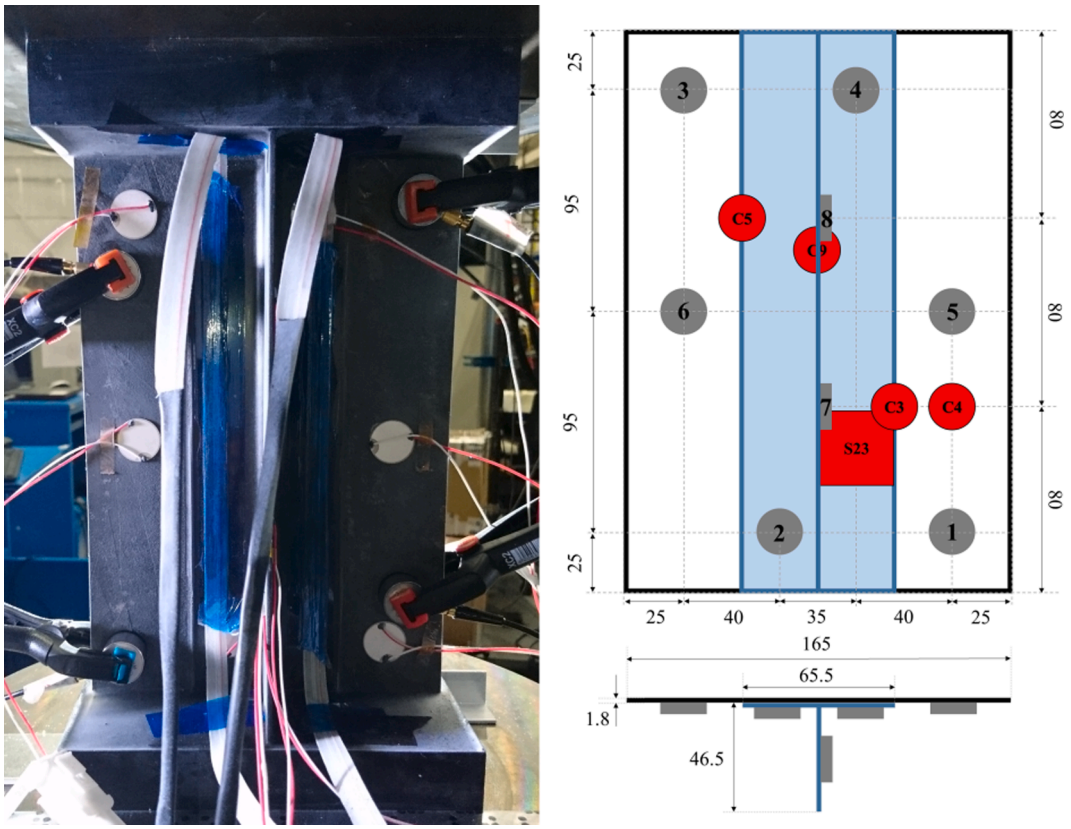

Fig. 1. Stiffened panel and dimensions in mm. The piezoelectric sensors are marked by grey circles (1 to 8). The impact damage locations on panels C3, C4, C5 and C9 are indicated by red circles. The Teflon insert on panel S23 is marked red rectangle. (For interpretation of the references to colour in this figure legend, the reader is referred to the web version of this article.)

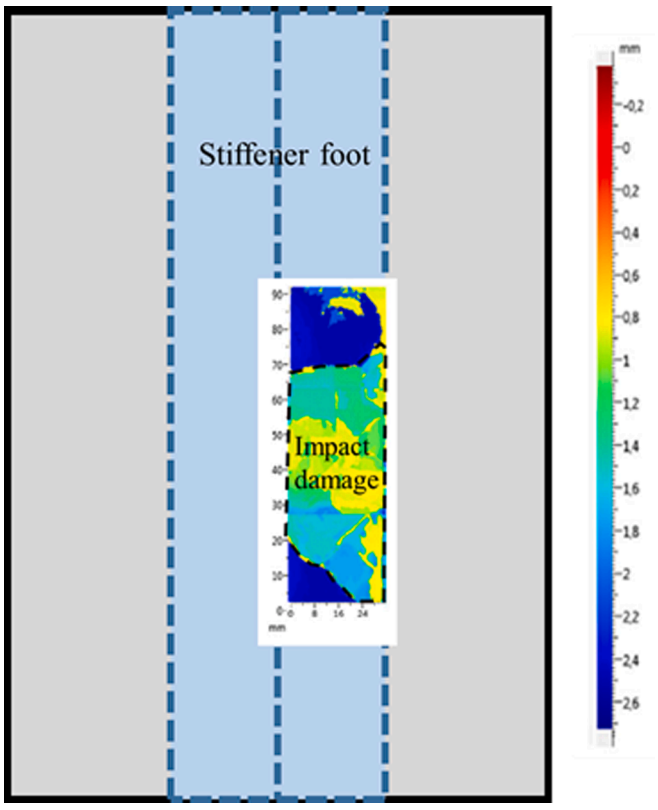

Fig. 2. C-scan image after 10 J impact on the stiffener foot from the skin side. [31].

panel. The damage locations are shown in Fig. 1.

Prior to fatigue, the buckling load and ultimate compressive load are assessed with a quasi-static compression test of a pristine panel, which was estimated at 12.8kN and 104kN, respectively. The stiffened panels are tested under compression-compression fatigue until failure with maximum load around 50–65% of the ultimate load and load ratio of 0.1. The stiffness of the specimens at pristine conditions are estimated using 7 nominally identical specimens without PZT sensors tested under quasi-static loading prior to impact.

The details of the five PZT sensorised stiffened panels are summarised in Table 1. Panels C3, C4, C5 and C9 were impacted and tested under constant amplitude fatigue loading at 65% of the ultimate load. Panel S23 has a Teflon insert under the foot of the stiffener and was tested under increasing step loading at 50% for 100,000 cycles and then at 60% until failure. Fig. 3 shows the stiffened composite panel prior to testing in pristine condition, and after failure with a close-up of the failure region. Additionally, the skin-stiffener region has disbonded.

Each stiffened panel is monitored using five systems: acoustic emission (AE), distributed Rayleigh-backscattering fiber optic strain sensing, fiber Bragg grating (FBG), guided waves and digital image correlation (DIC). To allow for measurements by each technique, the fatigue load is paused at pre-defined intervals. The fatigue load cycle is interrupted every 500 cycles except for the 5000th cycle, and the panel is subjected to quasi-static loading from the minimum to the maximum fatigue load level under a constant displacement rate of 0.5 mm/min. The FBG and DIC systems take measurements throughout the quasi-static loading, while the distributed strain is recorded at the minimum and maximum load. After every 5000 fatigue cycles, the applied load is reduced to 0 kN to allow for GW measurements. Finally, the AE system is continuously recording throughout the load cycle. For this work, only data recorded by the guided waves and DIC systems are studied. Readers may refer to [32] for the detailed description of other systems. The dataset used in this work is publicly available at [33].

Table 1
Test details.

Specimen		Damage	Damage location	Maximum compressive load (kN)	Cycles to failure
Constant amplitude loading	C3	10 J Impact	stiffener skin	65	152,458
	C4				280,098
	C5		stiffener		144,969
	C9		stiffener		133,281
Step loading	S23	Disbond of stiffener foot using Teflon insert	stiffener	50 and 60	438,000

Guided waves are excited at frequencies of 50, 100, 125, 150, 200, 250 kHz by applying a 5-cycles tone burst signal on one PZT sensor and are acquired using the other PZT sensors. The guided waves signals are recorded in a round robin way, where each PZT acts sequentially as transmitter and receiver. Each signal is recorded 10 times and averaged for noise reduction.

The DIC images of the skin side are recorded using a Correlated Solutions system with two 5 Mega pixel cameras and 50 mm lenses. The image taken before impact at 0 kN is used as the reference image for post-processing.

During the fatigue testing, the ambient temperature in the laboratory is not controlled. At the time of testing the daily temperature variation is within 3℃ in December at Delft, Netherlands [34]. The longest of fatigue testing on panel S23 lasted seven consecutive days and the temperature variation in the laboratory is expected to be less than the outdoor air temperature. Hence the greatest temperature variation should not exceed 5℃ for each panel.

3. Post-buckling fatigue degradation

Understanding the post-buckling behaviour and the fatigue degradation phenomenon of the stiffened panels is essential to provide guidance to guided wave processing and interpretation.

A half wave buckling pattern is observed for the 5 stiffened panels with two opposite buckling directions, as shown in Fig. 4. Panel C3, C4 and C5 showed clockwise buckling of the skin and stiffener flange, while Panel C9 and S23 showed anti-clockwise buckling of the skin and stiffener flange. The side of the panel where the skin is moving away from the stiffener foot (opening side) is dominated by Mode I fracture, while the other side where the skin is moving towards the stiffener foot (closing side) is dominated by Mode II fracture. The disbond and delamination is likely to propagate along the axial direction, and propagates easier under Mode I than Mode II.

Fig. 5 shows the out-of-panel displacement (W) and the axial in-plane strain (ε_{yy}) of the panel skin at the maximum compressive load. The value at the first quasi-static loading and the last quasi-static loading before failure are noted by subscript 1 and N-1, respectively. Both W_1 and ε_{yy1} are similar among all panels despite the difference in BVID or disbond location, which indicates that the difference in initial damage locations doesn't immediately affect the strain distribution of the structure.

The out-of-panel displacement (W) is antisymmetrically distributed and its magnitude increased at the end of the fatigue life. For the panels where the initial damage is located on the stiffener foot at the opening side (C5 and S23), the W distribution increased towards initial damage location, indicating an increase of damage size. The asymetric distribution of axial in-plane strain (ε_{yy}) is caused by the antisymmetric deformation. On the side where the skin is moving towards the DIC camera (i.e. away from the stiffener, refered to as opening side), the compressive strain on the skin surface is released, thus showing lower ε_{yy} compared to the middle of the panel. While on the opposite side of the panel where the skin is moving away from the DIC camera (i.e. towards

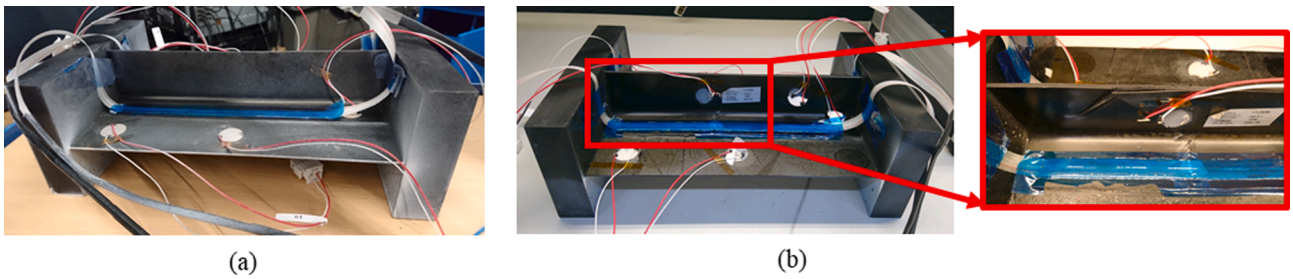

Fig. 3. Stiffened composite panel (a) in pristine condition prior to testing and (b) after failure with a close-up of the failure region.

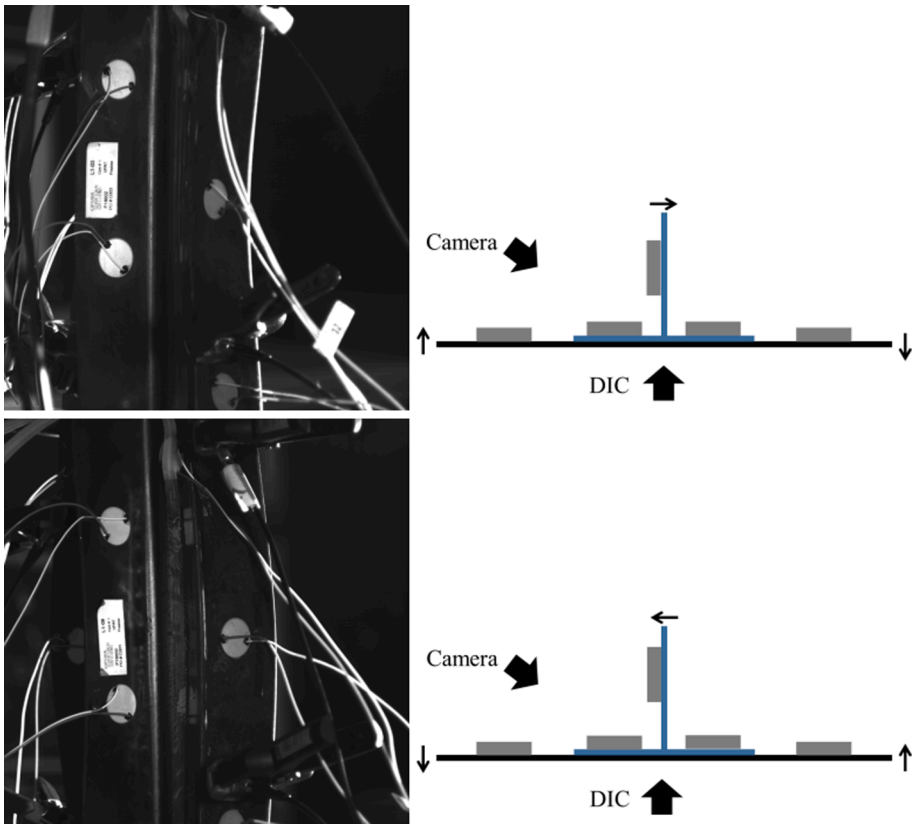

Fig. 4. Buckling and deflection direction shown for the cross section together with camera images taken from the side. Clockwise (top) and anti-clockwise (bottom) as seen from the top.

the stiffener, refered to as closing side), the compressive strain on the skin surface is superimposed, thus showing higher ε_{yy} compared to the middle of the panel.

It can be seen that the deformation and strain under fatigue loading increase and redistribute under fatigue loading, but the redistributions are not always correlated with the initial damage locations. This suggests that the fatigue degradation happens globally in the structure and the initial damage doesn't always grow under fatigue.

The load–displacement curves during quasi-static loading are shown in Fig. 6(a). The buckling load of the coupons lies between 12kN and 16kN. A nonlinear region of the load–displacement curve can be seen from 10kN to 40kN, which might be caused by the emergence of buckling. The stiffness is estimated by the slope of linear regression of the linear region of the load–displacement curves, which is 5kN to 10kN for pre-buckling and 40kN to 60kN for post-buckling. The stiffness history of the 5 panels listed in Table 1 are shown in Fig. 6 (b) and (c). The pre-buckling and post-buckling stiffness history are similar in trend, while the former shows higher values than the latter. The initial and failure values of the stiffness are similar among the 5 panels for both cases.

In contrast to the typical three-phase S-shaped stiffness degradation in the T-T fatigue, there is no rapid initial degradation phase in the C-C fatigue in case of the stiffened panels, but the phase II and phase III are comparable, which has also been reported for simple coupons in [5,6]. The stiffness history needs to be normalised for comparison with the guided waves results in this work. However, as the specimens are impacted or artificially disbonded in various locations prior to fatigue testing, the initial stiffness obtained during the test might have been affected by the damage and thus cannot be used for normalisation. To estimate the pristine stiffness, 7 nominally identical specimens from the test campaign (without PZT sensors) are used. These 7 specimens are tested under quasi-static compression with the same loading range and rate at pristine state and their load displacement curve are used to estimate the pristine stiffness. The average and standard deviation of the pristine stiffness across the 7 specimens is 51.9 kN/mm and 0.39 kN/mm, respectively.

The consistency of the initial deformation distribution and the initial stiffness among the panels despite the difference in BVID and disbond

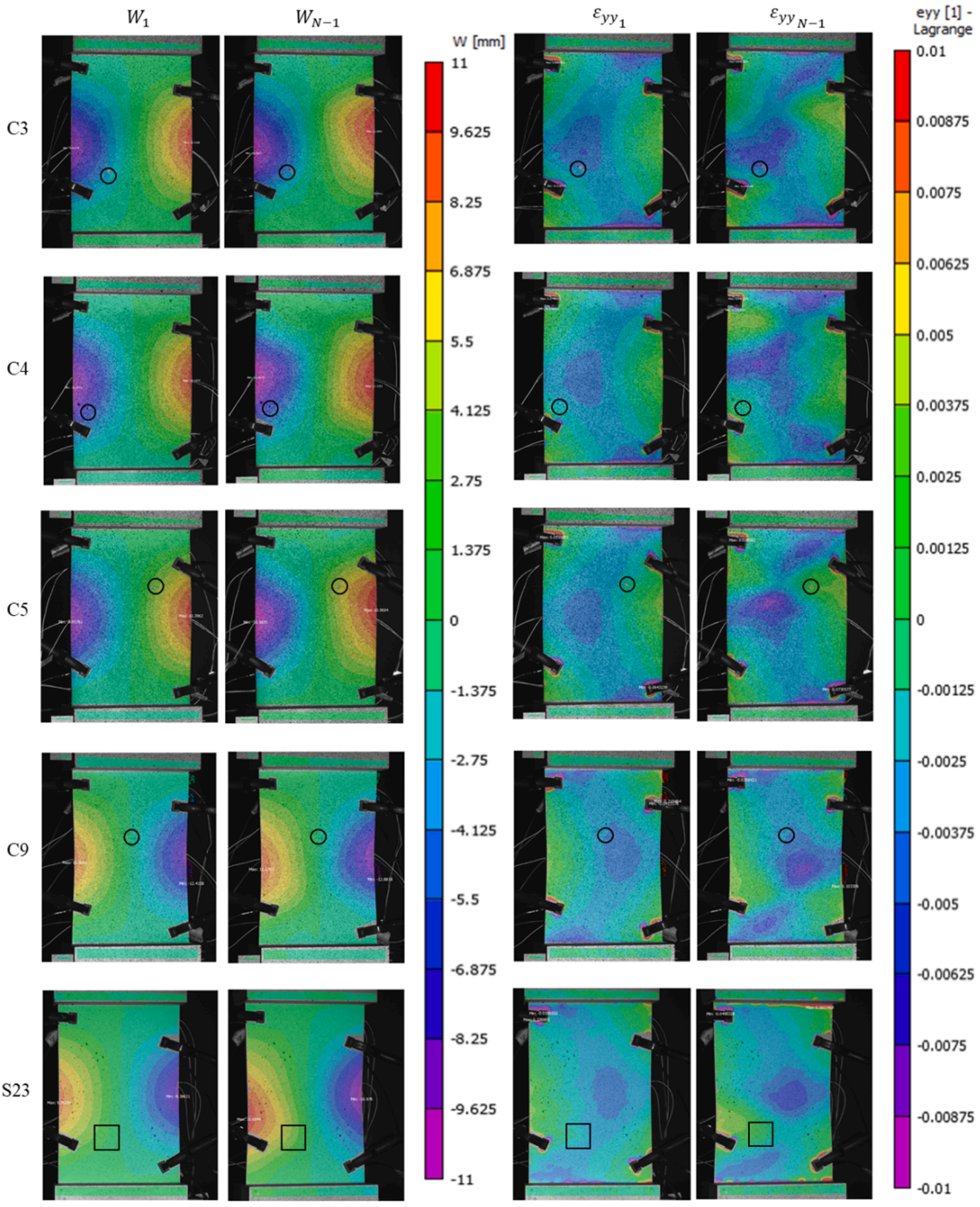

Fig. 5. DIC images of five panels at maximum compressive load with the same scale. The warm colours indicate positive deformation, e.g., towards the camera or expansion. The cool colours indicate negative deformation, e.g., away from camera or compression. The initial damage location is marked by solid black line.

position indicates that the local damage doesn't immediately influence the global load bearing capacity. However, the difference in the length of fatigue life can be observed among the four panels impacted at different locations. As the stiffener is the main load bearing structure, the integrity of stiffener-skin bonding is crucial to fatigue performance. C9 has the shortest fatigue life as the BVID is on the stiffener-skin bonding. C3 and C5 have similar stiffness history and they are both impacted on the edge of the stiffener. C4 has the longest fatigue life as the impact is on the skin, which has minimal influence on the stiffener. Our colleagues Broer et al [32] monitored the skin-stiffener disbond and stiffness degradation of panel C3, C4 and C5 using distributed fiber optic strain sensing along the two feet of the stiffener. Early disbond growth was observed in C3 at BVID location but no stiffness degradation was detected, while later in the fatigue life, stiffness degradation was observed prior to the disbond growth. For C4, stiffness degradation was observed throughout the fatigue life but the disbond growth was only seen near the end of the fatigue life. The two phenomena were observed simultaneously for C5.

One hypothesis for fatigue damage mechanisms of the stiffened panels under C-C fatigue loading would be that the accumulation of local damage, especially the disbond growth, causes localized decrease of stiffness of the surrounding structure and leads to global stress redistribution, which then stimulates the damage to accumulate globally in the weak locations (e.g., matrix cracking) of the structure and results in

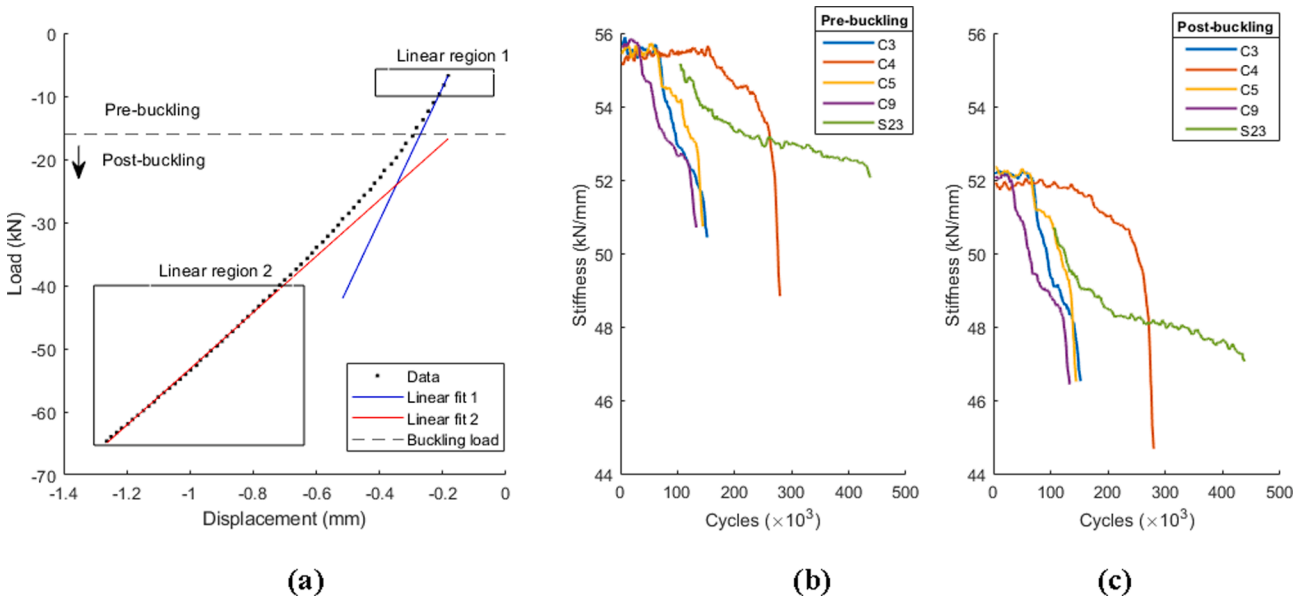

Fig. 6. (a) Load vs displacement curves recorded during quasi-static loading of Panel C3. (b) Pre-buckling and (c) post-buckling stiffness of the five coupons.

global stiffness degradation. The global stiffness degradation, in turn, leads to greater axial displacement and buckling deflection, which stimulates the accumulation of damage globally. In this sense, the stiffness degradation can trigger disbond growth but the disbond growth should not immediately cause stiffness degradation. On the other hand, the axial stiffness degradation leads to the increase of deflection, which causes the accumulation of matrix cracking in the entire panel. In other words, the accumulation of matrix cracking could be representative of axial stiffness degradation.

4. Stiffness degradation assessment using guided waves

This section presents the key steps and considerations in the assessment of stiffness degradation using guided waves including sensor path selection, guided wave mode selection, phase velocity calculation considering sensor failure and wave mode conversion, and global stiffness estimation using multiple frequencies. The method development is demonstrated using the guided waves signals recorded on panel C3.

Various features in time domain, frequency domain as well as time–frequency domain can be extracted to characterise the changes occurring in guided waves during the damage evolution process. However, selecting the most appropriate features is not an easy task due to the complexity of the change observed in guided waves signals as the result of the complex changes in the structure, the PZT sensors and their bonding. Previous experimental studies on guided waves-based fatigue damage accumulation have shown that the reduction in phase velocity is closely correlated to the stiffness degradation of simple specimens under T-T, T-C and C-C fatigue load [5,22,35]. Numerical and analytical studies have also demonstrated the influence of changes in material properties on the phase velocity [18,19]. The phase velocity of the first arriving wave mode can be related to the structural degradation in the direct path of the wave propagation, which is practical and reliable when multiple modes coexist and overlap. Therefore, in this work, the phase velocity of the first arriving wave mode is used to estimate stiffness degradation. It is considered that the accumulation of fatigue damage causes the degradation in the Young's modulus (as shown in Fig. 6) which leads to the reduction of the guided waves phase velocity.

4.1. Sensor network and path selection

As discussed in Section 3, the global matrix cracking accumulation and localised disbond growth are likely to be the two dominant damage mechanisms in post-buckling fatigue, and the former could be more representative of the global axial stiffness degradation than the latter. Thus, the selection of guided waves paths should be distributed over the panel rather than localized around the initial damage location where disbond growth is likely to occur. In the post-buckling fatigue, the deflection (as shown by DIC in Fig. 5) is likely to introduce matrix cracking perpendicular to the axial direction. Therefore, the signal paths predominantly along the loading axis are selected to assess the axial phase velocity, as shown in Fig. 7.

As the buckling of the panel under compression loading is anti-symmetric and the positions of the initial damage locations varies from panel to panel, the stress distribution and the damage accumulation can be asymmetric within each panel and differs from panel to panel. Therefore, the panels are partitioned into three sections, namely left, middle and right (seen from the skin side), and the quasi-axial signal paths within each section are selected to assess the axial modulus, as shown in Fig. 7. The reciprocal path is considered for each transducer pair to capture the modulus from the reciprocal wave propagating directions, even though the values are expected to be similar.

4.2. Guided wave mode selection

Fig. 8 shows the pre-processed signals recorded after impact at 0, 5000, 10,000 and 15,000C-C fatigue cycles. The signals recorded at path 1–5 and path 2–4 are shown, which are on the skin and the skin-stiffener bonding, respectively. The recorded guided wave signals are averaged over 10 repetitions and filtered using Morlet wavelet at the excitation frequency. Two fundamental wave modes can be observed at the first arrival of the signals over the acquired frequency range. The fundamental asymmetric (A0) mode is mainly seen at 50 kHz and the fundamental symmetric (S0) mode exists at higher frequencies. The arrival time of S0 mode is similar from 100 kHz to 250 kHz and reaches the maximum amplitude between 125 kHz and 150 kHz.

The change in amplitude and phase of the guided wave signals can be observed at all acquired frequencies, while more changes are seen at 50 kHz to 150 kHz compared to 200 kHz and 250 kHz. Large deviation of the signals is observed at early fatigue life between 0 and 10,000 cycles. Similar phenomenon has been reported for T-T fatigue in [22] and the large changes in phase velocity at initial fatigue loadings were attributed to the fibre breakage. However, in the C-C fatigue, the fibre breakage is

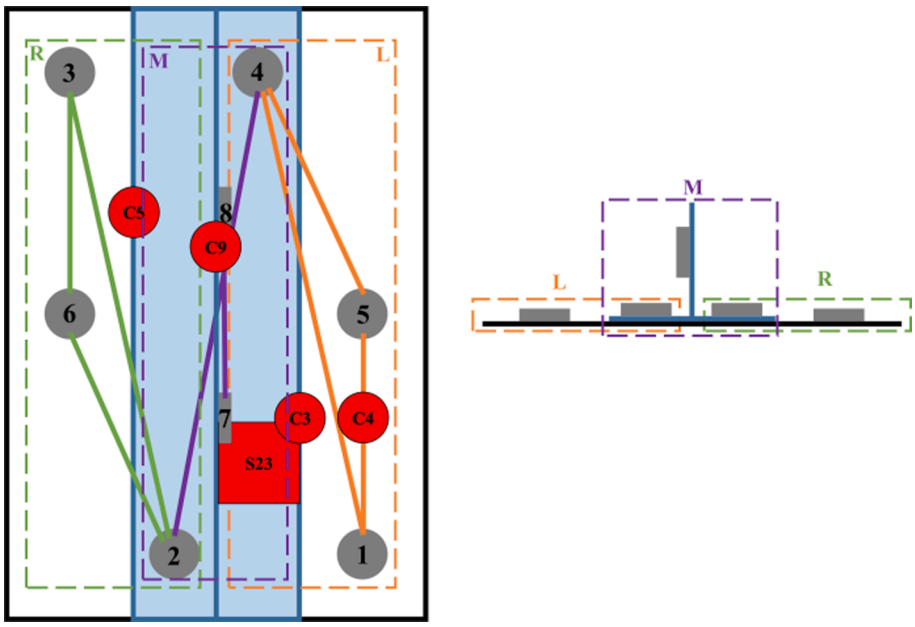

Fig. 7. Sensor path selection for stiffness degradation assessment. The panel is partitioned into left (L), middle (M) and right (R) sections with dash lines, as seen from the skin (DIC) side. The sensor paths within each section are plotted with the corresponding colour of the section.

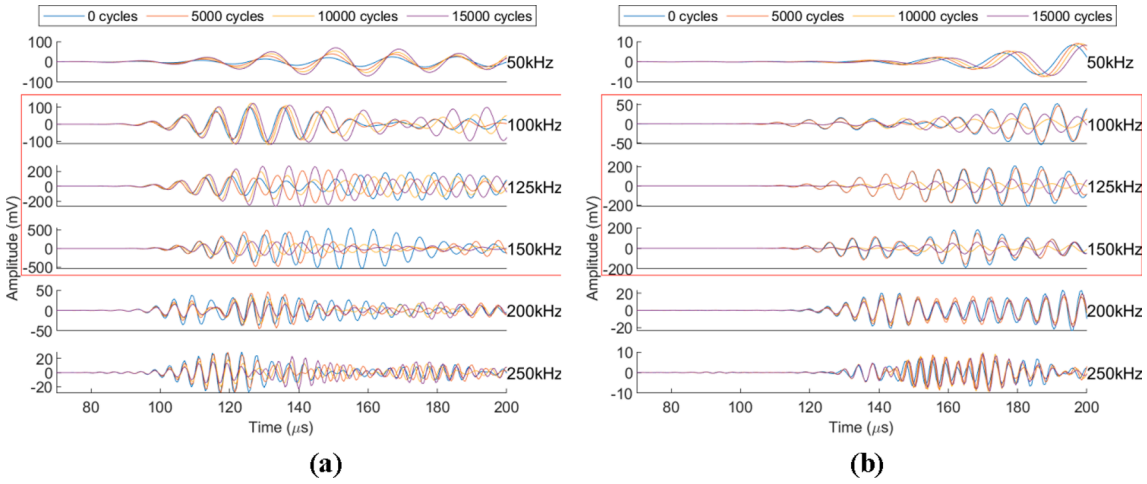

Fig. 8. Guided wave signals at 0, 5000, 10000, 15000 C-C fatigue cycles recorded by (a) path 1–5 and (b) path 2–4. Signals at 100 kHz, 125 kHz and 150 kHz are selected for this work (marked with red rectangles). (For interpretation of the references to colour in this figure legend, the reader is referred to the web version of this article.)

unlikely to occur at the initial fatigue loading, and this large change in the signals is believed to be the results of the release of residual stress introduced in the curing process and by manufacturing defects. Wave mode conversion behavior is also observed at multiple frequencies, where the first arriving waveform is no longer consistent. In those cases, the phase velocity before and after the mode conversion is no longer comparable, and the adjustments are discussed in Section 4.4. Signal amplitude reduction to the noise level, i.e. signal absence, is also observed, which is related to PZT fracture or disbond. This is also discussed in Sections 4.6 and 4.7.

On the choice of guided wave mode, Tao et al. [22] pointed out that the dispersion curve of S0 mode is nearly flat in the low frequency thickness product region, indicating that the phase velocity is almost insensitive to the thickness or frequency, and thus depicts a quasi-nondispersive behavior which is beneficial for material characterization purposes. The use of the S0 mode allows flexibility in the excitation frequency and it is also the fastest mode which is convenient in practice. Another benefit of using the S0 mode is that the relation of phase velocity and axial Young's modulus can be derived at low frequency thickness product.

At low frequencies Lamb waves can be well approximated by plate theory. According to Poisson theory (the lowest order plate theory), the dispersion equation of S0 mode is [36].

$$\omega^2 = \frac{E}{\rho(1-\nu^2)}k^2 \tag{1}$$

where E, ρ and ν are Young's modulus, density and Poisson's ratio of the medium, respectively. ω, k are the circular frequency and wavenumber of the wave. As S0 mode is nondispersive in the low frequency thickness product region, the phase velocity (C_p) and group velocity (C_g) can be written as [22].

$$C_g = C_p = \sqrt{\frac{E}{\rho(1-\nu^2)}} \tag{2}$$

To validate the approximated expressions in the frequency range concerned in this work, the dispersion curves for the material and thickness used are derived, and the approximated expression (Equation (2) is plotted against the exact solutions in Fig. 9. It can be seen that the approximated expressions match well with the exact S0 mode solution of phase velocity and group velocity, which confirms the validity of Equation 2 for this work.

The Young's modulus can then be estimated using a low frequency S0 mode phase velocity as.

$$E = \rho(1-\nu^2)C_p^2 \tag{3}$$

Assuming the change in density and Poisson's ratio is negligible, the degradation of the axial modulus can be described by.

$$D = \frac{E}{E_0} = \left(\frac{C_p}{C_{p0}}\right)^2 \tag{4}$$

where C_{p0} denote the S0 mode phase velocity at pristine condition.

Considering the stronger response, flexibility in frequency selection, and convenience in material characterization of S0 mode, S0 mode dominant guided waves response at 100 kHz, 125 kHz and 150 kHz are considered in this work, as marked in Fig. 8.

4.3. Phase velocity calculation and validation

Since the S0 mode is almost non-dispersive at the selected frequencies, the phase delay of the signal can be calculated using cross correlation between the reference signal $S_r(t)$ and the current signal $S_c(t)$. It should be noted that cross correlation can be used to derive phase changes of the signals only if the guided wave is non-dispersive, i.e., phase velocity equals group velocity.

Considering only the first arriving mode for phase delay, the reference signal is windowed from the start until the third peak within the first wave packet. This time window is denoted as τ. The phase delay is determined by the lag δ of the reference signal corresponding to the maximum cross correlation with the current signal:

$$\delta = \text{argmax}_\delta \; xcorr\left[S_{rf}^{\tau}(t+\delta), S_c(t)\right] \tag{5}$$

where *xcorr* denotes cross correlation.

The first arriving wave mode can change significantly due to damage accumulation and degradation in material properties during the fatigue loading. Fig. 10 shows the phase delay in specimen C3 on path 1–5, 6–3 and 7–8, where three representative signal history throughout the fatigue life can be seen. Path 1–5 has consistent wave mode throughout the fatigue life. Path 6–3 sees wave mode conversion from S0 mode to A0 mode, and the signals after wave mode conversion are plotted in Fig. 10 (d) with the first converted signal plotted in bold red line. path 7–8 has consistent wave mode until the failure of PZT 7 which leads to the absence of the signal. Nevertheless, the phase delay of the first arriving wave mode is only meaningful if the signal is valid and the wave mode is consistent. To validate the consistency of the wave mode, the current signal is shifted back with the determined phase delay to check the consistency of its waveform with the reference signal, as shown in the lower part of Fig. 10.

The correlation coefficient (CC) between the current signal shifted back by the phase delay and the reference signal is computed to measure the similarity:

$$CC = corr[S_c(t-\delta), S_r(t)] \tag{6}$$

where *corr* denotes correlation coefficient and $-\delta$ indicates the shift of the current signal. The threshold of CC for a consistent wave mode is set to 0.92, which is determined manually from multiple signal paths over several specimens. If CC falls below the threshold, it is considered that mode conversion occurs.The fracture and disbond of the PZT sensors during the fatigue loading causes large amplitude drops or absence of the transmitted or received guided waves signals. To ensure the validity of the recorded guided waves signal, the energy ratio (ER) of the current signal $S_c(t)$ to the reference signal $S_r(t)$ within the time window τ is calculated as:

$$ER = \frac{\sum S_c^{\tau}(t)^2}{\sum S_r^{\tau}(t)^2} \tag{7}$$

The threshold of ER is set at 0.2 above which the signal is considered valid. The threshold value is obtained by comparing the ER from intact PZTs and disbonded PZTs confirmed by visual observation during fatigue loading.

The determined phase delay is considered meaningful only if ER and CC are above their corresponding threshold. The phase velocity is then calculated as:

$$C_p = \frac{d}{t_0 + \delta} \tag{8}$$

where d is the distance of the PZT sensor pair, t_0 denotes the time of flight of the reference signal.

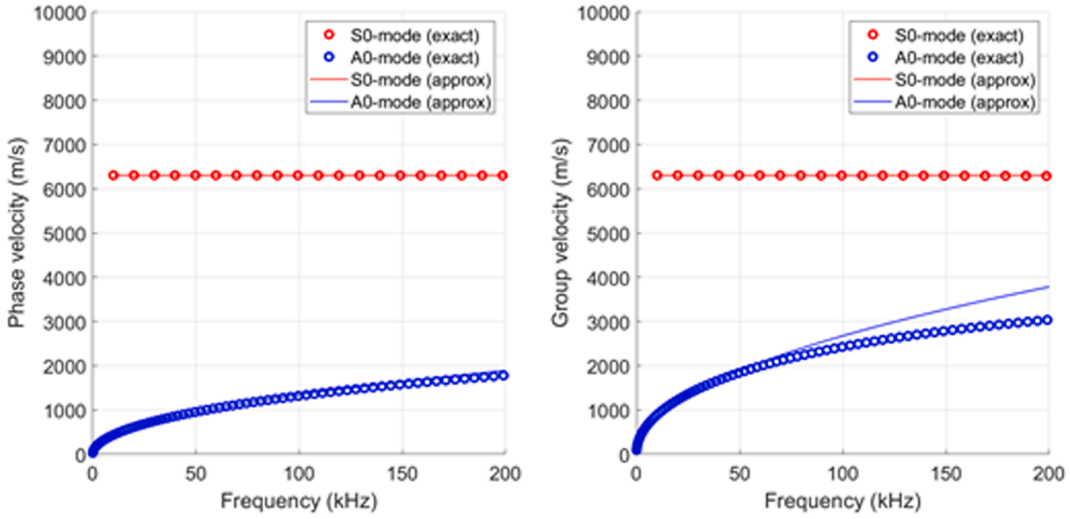

Fig. 9. Dispersion curves of the approximated solutions and exact solutions for the material and thickness used in this work.

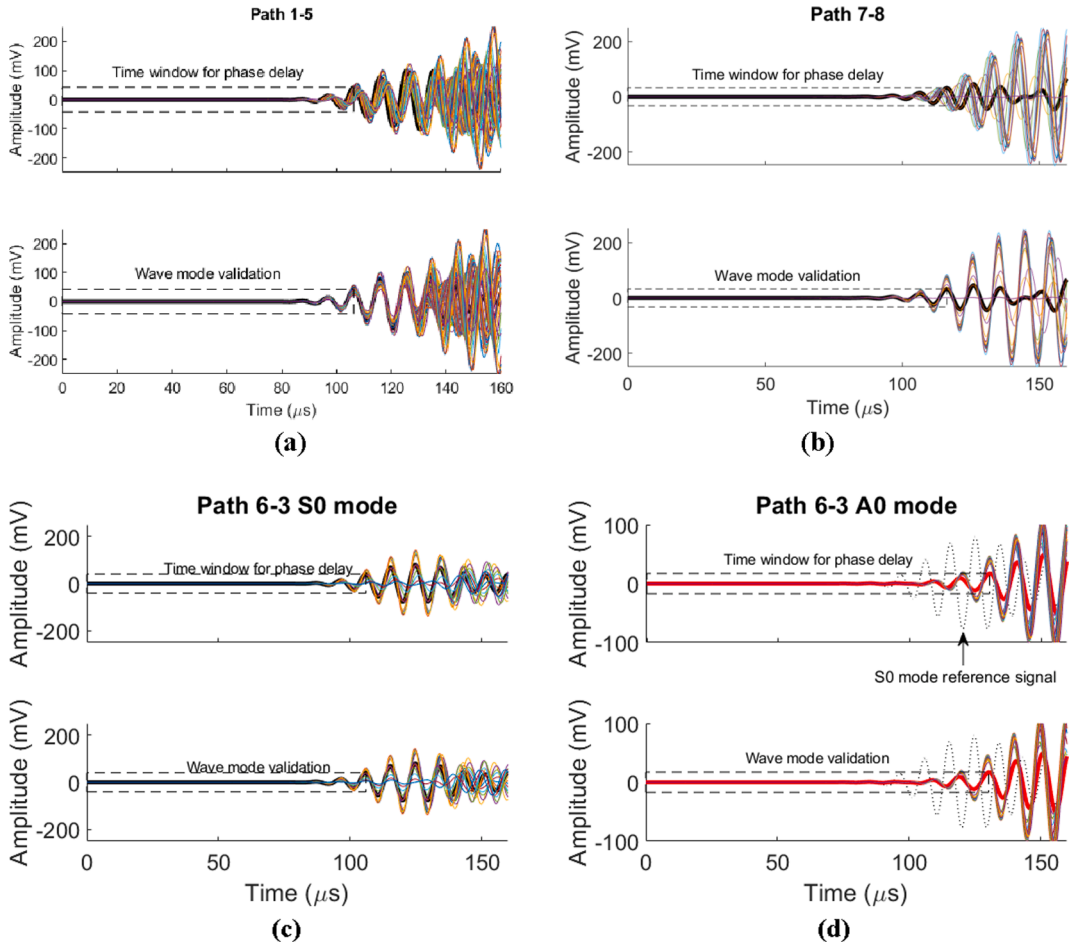

Fig. 10. Guide wave signals and wave mode validation in C3 path (a) 1–5 (b) 7–8 throughout fatigue loading (c) 6–3 before mode conversion (d) 6–3 after mode conversion. The reference signal for phase delay is plotted in a bold solid line.

Fig. 11 shows the phase velocity and the associated validation indices, ER and CC, in path 1–5, 6–3 and 7–8, where constant wave mode, wave mode conversion and sensor failure are observed, respectively.

4.4. Wave mode conversion

As shown in Fig. 11(d), when mode conversion occurs, the phase velocity changes significantly but this change cannot represent the change in modulus. In the case of mode conversion, S0 mode converts to A0 mode. Assuming that the converted A0 mode corresponds to flexural waves in the low frequency domain, according to Kirchhoff theory, the following dispersion relation holds [36].

$$\omega^2 = \alpha E k^4 \tag{9}$$

with.

$$\alpha = \frac{h^2}{3\rho(1-\nu^2)} \tag{10}$$

where h is the thickness of the medium. The phase velocity and group velocity can be written as.

$$c_g = 2c_p = 2k\sqrt{\alpha E} \tag{11}$$

According to the dispersion curves shown in Fig. 9, the approximated

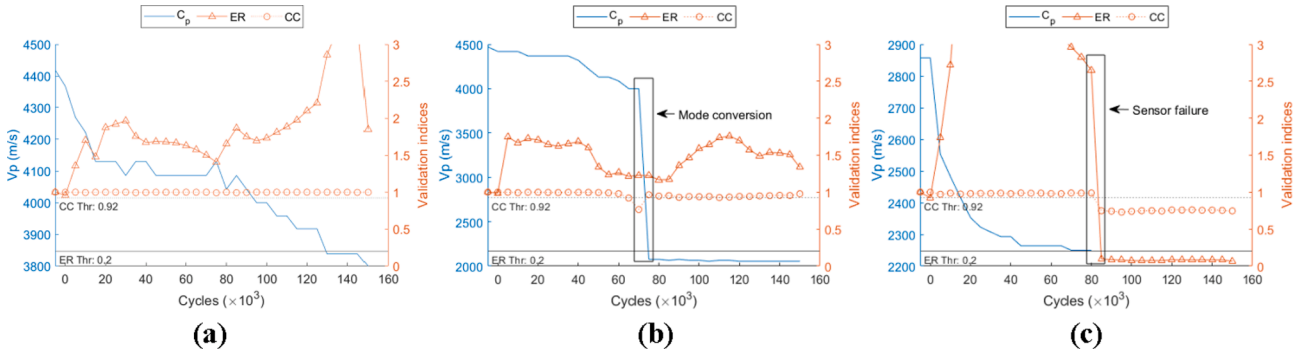

Fig. 11. Phase velocity and the associated validation indices CC and ER in C3 path (a) 1–5 (b) 6–3 (c) 7–8 throughout fatigue loading.

solution of A0 mode match well with the exact solution for phase velocity from 100 kHz to 150 kHz, while the approximated group velocity is only slightly higher than the exact solution towards 150 kHz. Thus the Young's modulus can be reliably estimated as.

$$E = \frac{c_g^2}{4k^2\alpha} = \frac{c_p^2}{k^2\alpha} \tag{12}$$

At a given frequency (and thus a given wavenumber k) and under the assumption that α is constant, the stiffness degradation can still be calculated by Equation (4).

To obtain the correct reference phase velocity value after mode conversion, the reference signal is changed to the first signal after mode conversion to determine the phase delay. Referring to Equation (4), the stiffness degradation can be written as.

$$D = \frac{E}{E_0} = \frac{E_1}{E_0} \bullet \frac{E}{E_1} = \left(\frac{C_{pk}}{C_{p0}}\right)^2 \bullet \left(\frac{C_{p1}}{C_{pk+1}}\right)^2 \tag{13}$$

where the subscript 0 denotes the initial wave mode, subscript k denotes the last recording of the initial wave mode, subscript k + 1 denotes the first recording of the converted wave mode, and C_{p1} denotes the phase velocity of the current wave mode. Therefore, the phase velocity ratio after mode conversion can be calculated as $\frac{C_{pk}}{C_{po}} \bullet \frac{C_{p1}}{C_{pk+1}}$.

4.5. Correction of large phase velocity ratio change

Fig. 12 (a-c) shows the phase velocity and the number of valid signal paths throughout the fatigue loading at 100 kHz, 125 kHz and 150 kHz. As the maximum stiffness degradation is approximately 0.85 as seen in Fig. 6(c), the minimum phase velocity ratio should be above 0.92 according to Equation (13). Since the stiffness should not increase during the fatigue loading, the phase velocity ratio should also not exceed 1. However, the calculated phase velocity ratio in several signal paths shows values as low as 0.3 and higher than 1.

The large drop of phase velocity ratio can be caused by the accumulation of local damage growth, such as skin-stiffener disbond growth. As discussed in Section 3, the local damage growth does not immediately affect the global load bearing capability (i.e. axial stiffness) and thus its influence should be excluded as it cannot represent the global stiffness degradation. To exclude large velocity value drops, the limit for phase velocity ratio change within 5000 cycles is set to 0.01. If the limited is exceed, it is considered that the phase velocity change is irrelevant and removed.

The increase in phase velocity ratio is unlikely to be caused by the increase of modulus, but instead by other factors such as noise or mode conversion. To avoid the increase in stiffness estimation due to the increase of phase velocity ratio, phase velocity ratio increases of more than 0.004 within 5000 cycles are excluded.

The corrected phase velocity ratios are presented in Fig. 12 (d-f).

4.6. Interpretation of sensor failure

As mentioned in the previous section, the failure of PZT sensors has been observed during fatigue loading and the phase velocity ratio from the corresponding sensor path becomes unavailable. Even though the degradation or failure of the PZT sensors is not a direct indication of structural damage or failure, it indicates that the strain at the PZT location is more detrimental to the PZT compared to the locations where PZTs are intact.

The threshold for ER is set using signals from disbonded PZTs in order to remove the invalid measurements. However, it should be noted that different types of PZT failure might have different effects on the guided waves signal response. For example, the PZT disbond leads to the absence of the signal while PZT fracture might only cause a drop in signal amplitude and the amplitude reduction could differ at different frequencies depending on the resonance frequency of the fractured PZT. Therefore, the ER reduction caused by a PZT disbond could be more significant than PZT fracture and the signal validity determined by ER can differ in different frequencies if the PZT is fractured but still bonded onto the structure.

In the absence of a valid phase velocity ratio, the material property at the signal path can no longer be indicated despite the potentially more

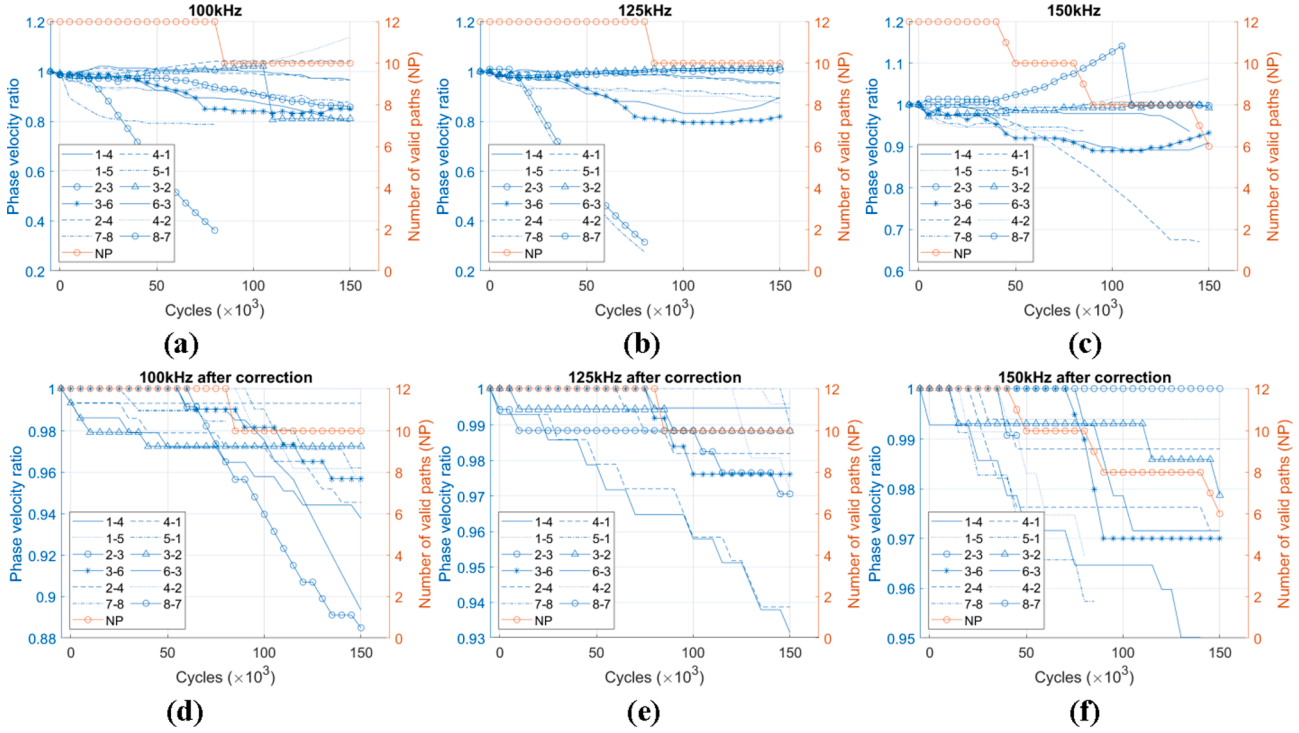

Fig. 12. Phase velocity ratio and number of valid signal paths throughout fatigue loading at (a) 100 kHz (b) 125 kHz and (c) 150 kHz, as well as the phase velocity ratio after correction at (d) 100 kHz (e) 125 kHz and (f) 150 kHz.

severe structural degradation. One option could be to extrapolate the values after sensor failure, but such extrapolation can lead to more erroneous results due to the lack of basis. However, the absence of the valid phase velocity value from some paths causes inconsistency in the overall stiffness estimation. Therefore, the phase velocity ratio is assumed to be maintained at the last available value prior to failure. However, this assumption can lead to the underestimation of stiffness degradation in the event of sensor failure. To indicate the validity of the estimation, the number of intact signal paths is noted throughout the fatigue life and serves as a weighting factor in the overall stiffness estimation.

4.7. Global stiffness degradation estimation

The axial stiffness of the structure at frequency f is estimated by the mean value of the selected paths:

$$\boldsymbol{D}^f = \overline{\boldsymbol{D}_p^f} \tag{14}$$

where D_p^f denotes the estimated axial stiffness degradation in path p at frequency f.

To estimate the global stiffness degradation, the phase velocity ratios at multiple frequencies are considered. The validity of the axial stiffness degradation estimation at each frequency is considered by the number of valid signal paths. The overall stiffness estimation is the average of the stiffness estimation at each frequency weighted by the number of valid signal paths w_f at corresponding frequencies:

$$\boldsymbol{D} = \frac{\sum_f \boldsymbol{w}_f \bullet \boldsymbol{D}_f}{\sum_f \boldsymbol{w}_f} \tag{15}$$

In the case of invalid stiffness estimation caused by PZT failure, the weighted average over multiple frequencies by the valid path number leans towards the estimation at the frequency where the most of the signal paths are valid. If no signal path is valid at all frequencies, the overall stiffness estimation becomes invalid.

5. Results and validation

5.1. Repeatability of guided wave response

To evaluate the repeatability of the guided wave response over the nominally identical panels, the first wave packet of the guided wave signals at 100 kHz from paths 1–5, 6–3, 7–8 and 2–4 are compared in Fig. 13 for the five panels at the pristine condition prior to testing. Consistent guided wave responses with similar amplitude and arrival time can be observed in the five panels. The small variations in the guided wave signals can be attributed to slight discrepancies in sensor locations and bonding condition caused by human error during sensor bonding procedure. An exception can be seen in Path 2–4 where the signal amplitude and arriving time for Panel S23 is significantly different from the other four panels. This is caused by the Teflon layer inserted under the stiffener foot in panel S23.

5.2. Axial stiffness degradation estimation

Fig. 14 presents the estimated axial stiffness degradation for 5 stiffened panels using sensor paths in the three sections (denoted by L, M, R as shown in Fig. 7) of the panel as well as using all the sensor paths (denoted by ALL). The estimation at 100 kHz, 125 kHz and 150 kHz as well as the weighted estimation over the three frequencies are presented for each case. To examine the between-path variations at each frequency, the standard deviation of estimated stiffness estimation among selected paths are plotted as shadow area at each frequency with the vertical length of the shadow area equal to the standard deviation value. It should be noted that the large value of standard deviation does not

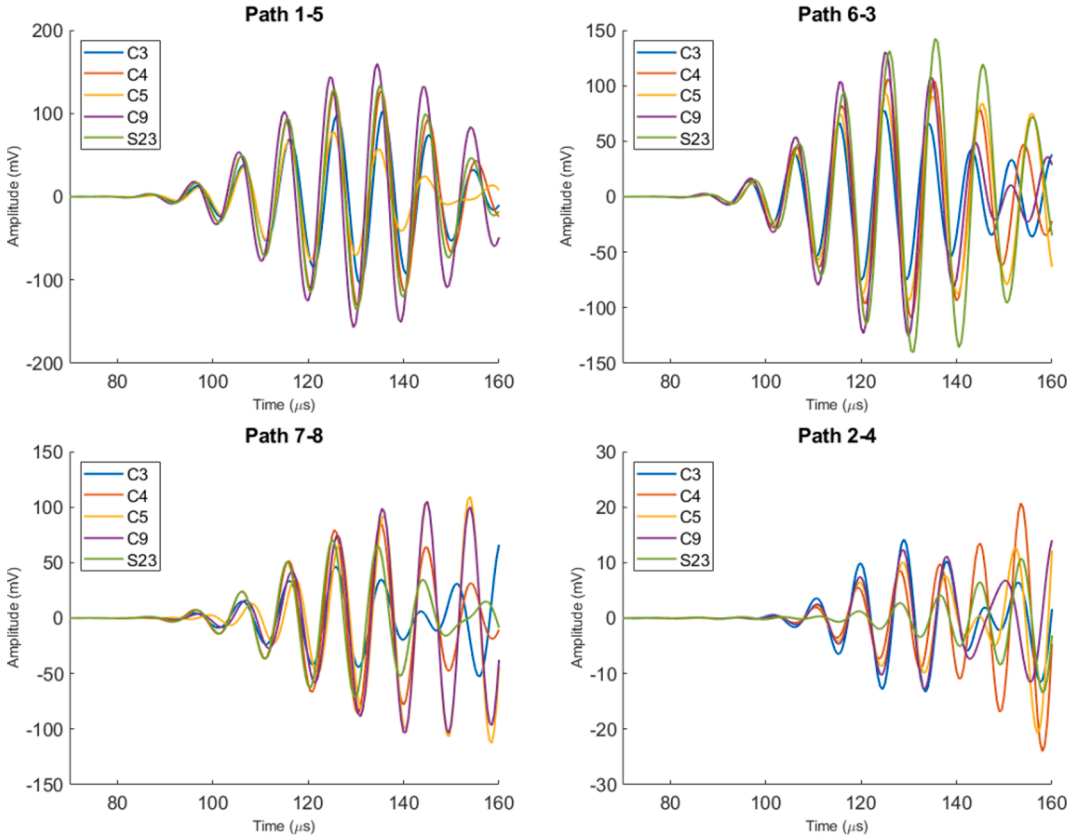

Fig. 13. Repeatability of guided wave signals on five specimens. Signals at 100 kHz from sensor paths 1–5, 6–3, 7–8 and 2–4 are plotted for comparison.

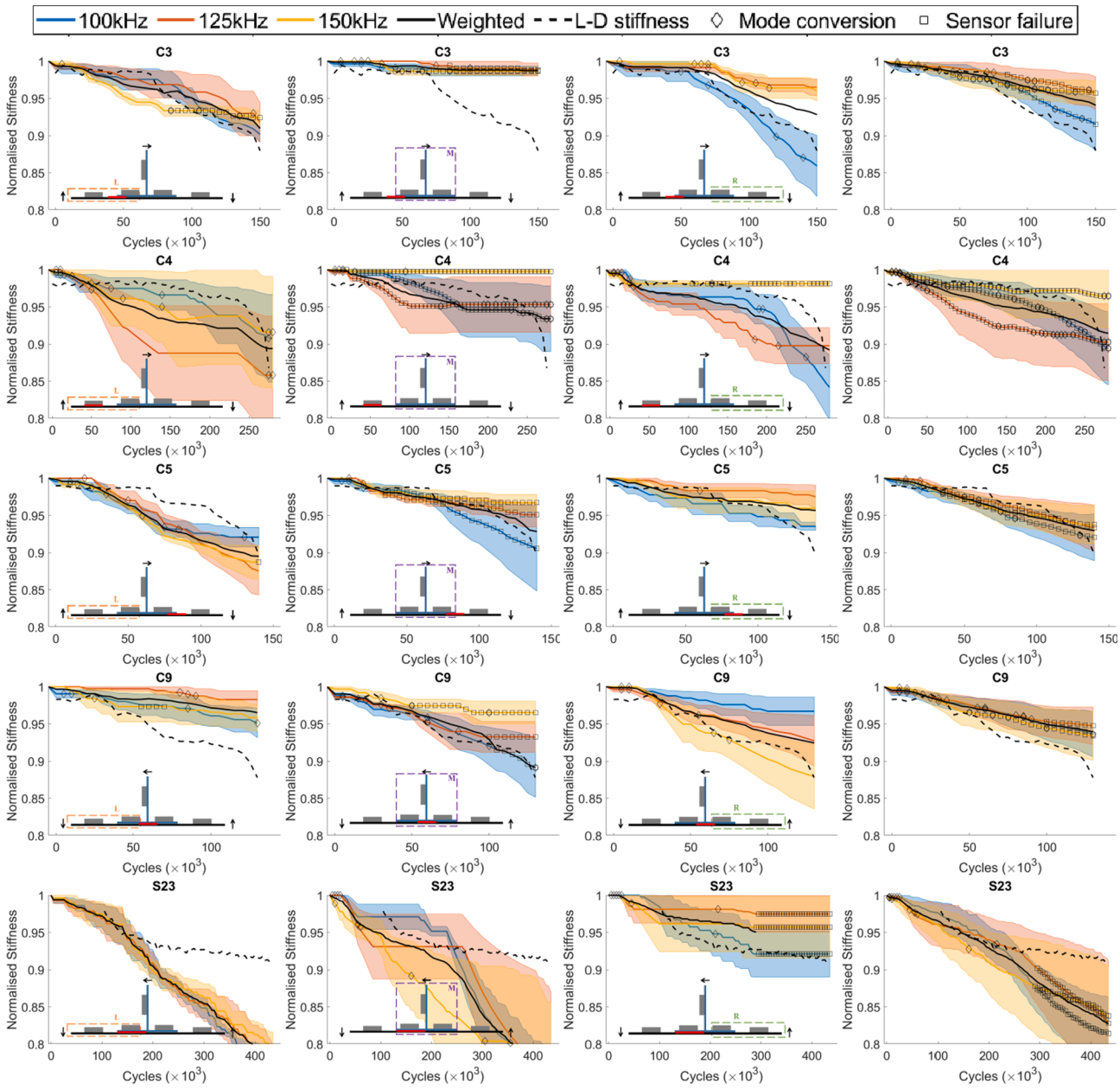

Fig. 14. Estimated axial stiffness degradation of stiffened panels. The normalized L-D stiffness (as shown in Fig. 6 (c)) is plotted for comparison. The first three columns show the result of L, M, R section of the panel, respectively. The last column shows the result of the entire panel using all sensor paths shown in Fig. 7.

indicate poor accuracy. Instead, it indicates the uneven spatial distribution of fatigue damage accumulation as well as its varied effect on different sensor paths, due to the globally distributed damage. For each frequency, the identified mode conversion and sensor failure behavior within the selected section are also indicated by diamond and square markers, respectively. The stiffness values measured from load-

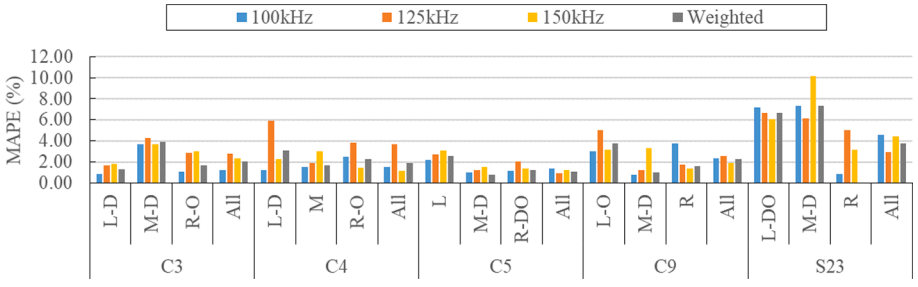

Fig. 15. MAPE of estimated axial stiffness degradation. The section that includes initial damage is denoted by D. The opening side (skin moves away from stiffener) is denoted by O.

displacement data (referred as L-D stiffness) shown in Fig. 6 in Section 3 are normalised by the average pristine L-D stiffness and plotted in dash line in Fig. 14 for comparison. For convenience of comparison, the reference value is interpolated at the cycle numbers where the guided waves signals are recorded.

Fig. 15 shows the mean absolute percentage error (MAPE) of the stiffness estimation with respect to the L-D stiffness value for the results presented in Fig. 14. The MAPE is calculated as.

$$\boldsymbol{MAPE} = 100\frac{1}{\boldsymbol{N}}\sum_{k=1}^{N}\left|\frac{\boldsymbol{x_k} - \widehat{\boldsymbol{x}}_{\boldsymbol{k}}}{\boldsymbol{x_k}}\right| \tag{16}$$

where x_k and $\widehat{x}_k$ are the reference and the estimated stiffness respectively, and N is the number of measurements.

Overall, the MAPE of the axial stiffness degradation estimation varies between 0.76% and 10.15%. The estimation for panels C3, C4, C5 and C9 are comparable while it's less accurate and overestimated for panel S23. This can be related to the types of initial damage. The Telfon insert under the stiffener during manufacturing (in S23) only introduced a disbond while the impact damage (in C3, C4, C5, C6) consists of a mixture of skin-stiffener disbond, matrix cracking, delamination and fibre breakage, which might have different influence on stiffness degradation as well as on guided waves propagation.

The estimation accuracy using different frequencies varies and none of the selected frequencies is consistently better than the others. The standard deviation among three frequencies at the same panel sections are also comparable. The weighted average of multiple frequencies reduces the MAPE from the maximum MAPE of using a single frequency and enhances the reliability.

The stiffness estimation at the left, middle and right section differ for each panel, one section might produce better estimation than the other (for example the left section of C3 and middle section of C5), but there is no consistent advantage regarding the initial damage location and the post-bucking deflection direction. Similarly, whether a section includes the initial damage location doesn't seem to have consistent influence on the estimated stiffness. This confirms the hypothesis that the stiffness degradation as well as the fatigue degradation is a global phenomenon. Although the local damage weakens the surrounding structure, the load bearing capacity of the structure is influenced by the continuous stress redistribution over the entire structure and should be assess globally rather than only around the local damaged area.

5.3. Prognostic performance metrics

As mentioned in Section 3, the stiffness shows comparable initial and failure values, and the rapid decreasing trend is consistently observed near the end of the fatigue life, which makes the stiffness a potential candidate as a prognostic health indicator. To have strong prognostic capability, a health indicator should display three features, namely monotonicity, trendability and prognosability [37]. The prognostic performance of axial stiffness is assessed next using these three features and a fitness function.

Monotonicity describes the general increasing or decreasing trend and is preferred as the degradation process is generally irreversible. Monotonicity can be calculated as.

$$\text{Monotonicity} = \frac{1}{\boldsymbol{M}}\sum_{j=1}^{M}\left|\sum_{k=1}^{N_j-1}\frac{\boldsymbol{sgn}\left(\boldsymbol{x_j}(\boldsymbol{k}+1) - \boldsymbol{x_j}(\boldsymbol{k})\right)}{\boldsymbol{N_j}-1}\right| \tag{17}$$

where x_j represents the vector of measurements of a feature on the j^{th} system, M is the number of systems monitored, and N_j is the number of measurements on the j^{th} system.

Trendability describes the similarity of the degradation process among multiple structures under the same loading scenario and is given as.

$$\textbf{trendability} = \min_{j,k}\left|\boldsymbol{corr}\left(\boldsymbol{x_j}, \boldsymbol{x_k}\right)\right|, \boldsymbol{j}, \boldsymbol{k} = 1, ..., \boldsymbol{M} \tag{18}$$

When x_j and x_k have different lengths, the shorter vector is resampled to match the length of the longer vector. To facilitate this process, their time vectors are first normalized to percent lifetime, that is, [0%, 100%].

Prognosability measures the similarity of the health indicator value at the event of failure and can be calculated as.

$$\textbf{prognosability} = \exp\left(-\frac{\boldsymbol{std_j}(\boldsymbol{x_j}(\boldsymbol{N}))}{\boldsymbol{mean_j}\left|\boldsymbol{x_j}(1) - \boldsymbol{x_j}(\boldsymbol{N})\right|}\right)\boldsymbol{j} = 1, ..., \boldsymbol{M} \tag{19}$$

A fitness function of prognostic performance metrices can be constructed by the combination of the three features. Considering the three features are equally important, thus giving equal weight of each feature, the fitness function can be written as:

$$\text{Fitness} = \text{monotonicity} + \text{trendability} + \text{prognosability} \tag{20}$$

The prognostic feature performance metrics of the reference stiffness and the guide wave estimated stiffness using all the selected sensor paths are listed in Table 2. The estimated stiffness at 100 kHz shows the best prognostic performance among the three frequencies, and the weighted estimation is better than the average performance and close to the best performing frequency. Compared to the reference stiffness, the estimated stiffness shows superior monotonicity and trendability but inferior prognosability. The relatively low prognosability of the estimated stiffness is related to the lack in capturing the rapid decreasing trend of stiffness near the end of the fatigue life. Nevertheless, the fitness of the estimated stiffness is higher than the reference at all frequencies, and is the highest at 100 kHz.

6. Discussion and future work

This work utilizes the guided waves phase velocity measured by a network of PZT sensors during C-C fatigue loading of stiffened panels to estimate the fatigue stiffness degradation. It is assumed that the global damage accumulation, primarily matrix cracking caused by post-bucking deflection, is representative of the global stiffness degradation, and that the global damage accumulation can be quantified using the reduction in guided wave phase velocity. It is considered that the local damage such as the skin-stiffener disbond does not immediately affect global stiffness degradation and thus is omitted in the estimation process. Although the aforementioned assumptions serve well in this work and led to coherent results, the understanding of the damage and failure mechanisms in C-C fatigue loading of CFRP structures is still limited, especially for post-buckling compression fatigue, which should be further investigated in the future.

The guided waves mode conversion behaviour has been observed during the fatigue loading, which is evidently caused by the damage accumulation. After mode conversion, as shown through Equations (10), the proposed approach to stiffness estimation still applies. In fact, the proposed approach is reliable even if the precise wave mode is unknown, as long as the mode conversion is identified and reference wave velocity correctly identified after mode conversion. The detailed study of the mode conversion behaviour is beyond the scope of this work, but could be an interesting topic for future work as suggested by [23].

In this work, the phase delay of the first arriving mode is calculated

Table 2
Prognostic feature performance metrics.

	L-D stiffness	100 kHz	125 kHz	150 kHz	Weighted
Monotonicity	0.66	1.00	1.00	0.92	1.00
Trendability	0.56	0.95	0.88	0.97	0.97
Prognosability	0.84	0.60	0.50	0.45	0.55
Fitness	2.06	2.55	2.38	2.34	2.52

using cross correlation of the signals. It should be noted that the cross correlation of signals is only appropriate for calculating phase change when the wave mode is non-dispersive. If the wave mode is dispersive, the cross correlation of the signals does not provide an accurate estimation of either phase or group velocity change. For dispersive wave mode, since the group velocity can also be used for stiffness estimation as shown in Equation (2) and (12), the cross correlation of the signal envelope can be used to calculate group velocity change in order to estimate stiffness degradation.

Similar to the fatigue degradation of the structures, the surface mounted PZT sensors also experience degradation under fatigue loading and hence inevitable failure. When the PZT sensors fail, the information from the associated area of the panel can no longer be acquired and leads to the missing of important damage accumulation information, especially near the end of the fatigue life. In this work, in order to reduce the influence of failed PZTs on the stiffness estimation, (1) the failed PZT sensors are identified and the phase velocity value of the associated signal paths are marked as invalid and (2) the validity of the stiffness estimation with respect to the state of the sensor network is considered by weighting the estimation over multiple frequencies by the number of intact sensor paths. Nevertheless, the sensor reliability is key to the effectiveness of the guided wave-based method, especially in fatigue related studies. The methods to improve sensor durability, as well as the redundant sensor placement, should be considered as a part of future works.

In some cases, the drop of stiffness near the end of the fatigue life is not captured by the guided waves, which can be caused by two reasons. The first reason could be that the damage mechanism changes near failure, such as compression instability or a quick stiffness drop caused by fast local disbond growth, which can no longer be represented by the global damage accumulation. The other reason is related to the inefficient sensor coverage near failure, which can be the result of either or both the PZT failure and the sensor placement. Therefore, how to design the sensor network to better capture the fatigue damage accumulation and failure mechanism should also be further investigated in the future.

In this work, the effect of temperature is neglected as the ambient temperature variation is small during the testing of each specimen (within 5℃). According to the experimental studies on similar CFRP materials in [15] and [38], the change in phase velocity ratio due to a 1℃ temperature change is between 0.001 and 0.0012, thus only a temperature change of 10℃ would be comparable to the phase velocity ratio change observed in this work (0.01 between two consecutive guided wave measurements at every 40 min). However, the effect of temperature cannot be neglected and should be compensated if the ambient temperature variation exceeds 10℃.

7. Conclusion

This work utilizes the guided wave phase velocity measured by a network of PZT sensors during post-buckling C-C fatigue loading of stiffened panels to estimate the fatigue stiffness estimation. The fundamental symmetric mode (S0) is selected for the estimation due to the multiple choices in frequency selection as well as the simplified relation of the phase velocity to modulus. Three frequencies and the weighted average are considered for stiffness estimation. The mode conversion and failure of PZT sensors are considered in the signal processing.

The axial stiffness is estimated using sensor paths in three sections of the panel as well as the entire panel, and there are no sections of the panel regarding the initial damage location and the buckling direction that consistently better represent the stiffness degradation, which indicates that the stiffness degradation is a global structural behavior and needs to be assessed globally. The weighted average estimation using all selected paths matches well with the reference value with the mean absolute percentage error between 0.76% and 10.15%. Regarding the potential of being used as a health indicator for prognostic purposes, the estimated axial stiffness is better in monotonicity and trendability but worse in prognosability than the reference axial stiffness. However, the overall prognostic fitness of the estimated axial stiffness is better than the reference, indicating a promising performance in prognostic applications.

CRediT authorship contribution statement

Nan Yue: Conceptualization, Methodology, Software, Validation, Formal analysis, Investigation, Writing – original draft, Writing – review & editing, Visualization. **Agnes Broer:** Conceptualization, Software, Data curation, Investigation, Writing – review & editing. **William Briand:** Software, Investigation, Writing – review & editing. **Marc Rébillat:** Formal analysis, Writing – review & editing, Resources, Funding acquisition. **Theodoros Loutas:** Writing – review & editing, Project administration, Resources, Funding acquisition. **Dimitrios Zarouchas:** Writing – review & editing, Resources, Funding acquisition.

Declaration of Competing Interest

The authors declare that they have no known competing financial interests or personal relationships that could have appeared to influence the work reported in this paper.

Acknowledgement

The authors acknowledge Embraer for the design of the structure, Optimal Structural Solutions for the manufacturing of the structure, CEDRAT Technologies for installation of the PZT sensors and for providing the Lamb Wave Detection System (LWDS), and our colleagues at Delft University of Technology and University of Patras for their technical support.

Funding

This work was supported by the European Union's Horizon 2020 research and innovation program (grant no.769288, ReMAP project).

References

[1] Alderliesten RC. Critical review on the assessment of fatigue and fracture in composite materials and structures. Eng Fail Anal 2013;35:370–9.
[2] Giurgiutiu V. Structural health monitoring of aerospace composites, London, UK: Academic Press is an imprint of Elsevier, 2015. [Online]. Available.
[3] Ansari MTA, Singh KK, Azam MS. Fatigue damage analysis of fiber-reinforced polymer composites—a review. J Reinf Plast Compos 2018;37(9):636–54.
[4] Li Xi, Kupski J, Teixeira De Freitas S, Benedictus R, Zarouchas D. Unfolding the early fatigue damage process for CFRP cross-ply laminates. Int J Fatigue 2020;140:105820. https://doi.org/10.1016/j.ijfatigue.2020.105820.
[5] Rheinfurth M, Kosmann N, Sauer D, Busse G, Schulte K. Lamb waves for non-contact fatigue state evaluation of composites under various mechanical loading conditions. Compos A Appl Sci Manuf 2012;43(8):1203–11.
[6] Liu H, Cui H, Wen W, Kang H. Fatigue characterization of T300/924 polymer composites with voids under tension-tension and compression-compression cyclic loading. Fatigue Fract Eng Mater Struct 2018;41(3):597–610.
[7] Uda N, Ono K, Kunoo K. Compression fatigue failure of CFRP laminates with impact damage. Compos Sci Technol 2009;69(14):2308–14.
[8] Saleh MN, El-Dessouky HM, Saeedifar M, De Freitas ST, Scaife RJ, Zarouchas D. Compression after multiple low velocity impacts of NCF, 2D and 3D woven composites. Compos A Appl Sci Manuf 2019;125:105576. https://doi.org/10.1016/j.compositesa:2019.105576.
[9] Saeedifar M, Saleh MN, El-Dessouky HM, Teixeira De Freitas S, Zarouchas D. Damage assessment of NCF, 2D and 3D woven composites under compression after multiple-impact using acoustic emission. Compos A Appl Sci Manuf 2020;132:105833. https://doi.org/10.1016/j.compositesa:2020.105833.
[10] Panettieri E, Fanteria D, Montemurro M, Froustey C. Low-velocity impact tests on carbon/epoxy composite laminates: a benchmark study. Compos B Eng 2016;107:9–21.
[11] Briand W, Rébillat M, Guskov M, Mechbal N. Upcoming damage size quantification in aeronautic composite structures based on imaging results post-processing. J Intell Mater Syst Struct 2022;33(2):251–65.
[12] Yue N, Khodaei ZS, Aliabadi MH. Damage detection in large composite stiffened panels based on a novel SHM building block philosophy. Smart Mater Struct 2021;30(4):045004. https://doi.org/10.1088/1361-665X/abe4b4.

[13] Yue N, Sharif Khodaei Z, Aliabadi FMH. An innovative secondary bonding of sensors to composite structures for SHM application. Key Eng Mater 2018;774:516–22.
[14] Yue N, Aliabadi MH. Hierarchical approach for uncertainty quantification and reliability assessment of guided wave-based structural health monitoring. Struct Health Monit 2020.
[15] Yue N, Aliabadi MH. A scalable data-driven approach to temperature baseline reconstruction for guided wave structural health monitoring of anisotropic carbon-fibre-reinforced polymer structures. Struct Health Monit 2019;19(5):1487–506.
[16] Gorgin R, Luo Y, Wu Z. Environmental and operational conditions effects on Lamb wave based structural health monitoring systems: a review. Ultrasonics Jul 2020;105:106114.
[17] Roy S, Ladpli P, Chang F-K. Load monitoring and compensation strategies for guided-waves based structural health monitoring using piezoelectric transducers. J Sound Vib 2015;351:206–20.
[18] Pant S, Laliberte J, Martinez M, Rocha B. Derivation and experimental validation of Lamb wave equations for an n-layered anisotropic composite laminate. Compos Struct 2014;111:566–79.
[19] Pant S, Laliberte J, Martinez M, Rocha B, Ancrum D. Effects of composite lamina properties on fundamental Lamb wave mode dispersion characteristics. Compos Struct 2015;124:236–52.
[20] Zhao J, Qiu J, Ji H. Reconstruction of the nine stiffness coefficients of composites using a laser generation based imaging method. Compos Sci Technol 2016;126:27–34.
[21] Giannakeas IN, Sharif-Khodaei Z, Aliabadi MH. "On the estimation of material properties using guided wave measurements for the calibration of finite element models," presented at the FRACTURE AND DAMAGE MECHANICS: Theory, Simulation and Experiment, 2020.
[22] Tao C, Ji H, Qiu J, Zhang C, Wang Z, Yao W. Characterization of fatigue damages in composite laminates using Lamb wave velocity and prediction of residual life. Compos Struct 2017;166:219–28.
[23] Zhang C, Zhang Z, Ji H, Qiu J, Tao C. Mode conversion behavior of guided wave in glass fiber reinforced polymer with fatigue damage accumulation. Compos Sci Technol 2020;192:108073. https://doi.org/10.1016/j.compscitech.2020.108073.
[24] Saxena A, Goebel Kai, Larrosa Cecilia C, Janapati Vishnuvardhan, Roy Surajit, Chang Fu-Kuo, Accelerated aging experiments for prognostics of damage growth in composite materials. In: Proceedings of the 8th International Workshop on Structural Heath Monitoring 2011, Stanford Univ., 2011: Destech Publications Inc.
[25] Mishra S, Vanli OA. Remaining useful life estimation with lamb-wave sensors based on wiener process and principal components regression. J Nondestruct Eval 2016;35(1). https://doi.org/10.1007/s10921-015-0328-2.
[26] Peng T, Liu Y, Saxena A, Goebel K. In-situ fatigue life prognosis for composite laminates based on stiffness degradation. Compos Struct 2015;132:155–65.
[27] C.R.L. Murthy, M.V. Hosur, T.S. Ramurthy, Compression after impact testing of carbon fiber reinforced plastic laminates, J. Compos. Technol. Res., 1999.
[28] ASTM D6641 / D6641M-16e2, Standard Test Method for Compressive Properties of Polymer Matrix Composite Materials Using a Combined Loading Compression (CLC) Test Fixture, 2016.
[29] Abramovich H, Weller T, Bisagni C. Buckling behavior of composite laminated stiffened panels under combined shear-axial compression. J Aircraft 2008;45(2):402–13.
[30] Kolanu NR, Raju G, Ramji M. A unified numerical approach for the simulation of intra and inter laminar damage evolution in stiffened CFRP panels under compression. Compos B Eng 2020;190:107931. https://doi.org/10.1016/j.compositesb:2020.107931.
[31] Galanopoulos G, Milanoski D, Broer A, Zarouchas D, Loutas T. "Health Monitoring of aerospace structures utilizing novel health indicators extracted from complex strain and acoustic emission data. Sensors (Basel), vol. 21, no. 17, Aug 24 2021.
[32] Broer A, Galanopoulos G, Benedictus R, Loutas T, Zarouchas D. Fusion-based damage diagnostics for stiffened composite panels. Struct Health Monit 2022;21(2):613–39.
[33] Zarouchas D, Broer A, Galanopoulos G, Briand W, Benedictus R, Loutas T. Compression Compression fatigue tests on single stiffener aerospace structures. Dataverse, NL; 2021.
[34] Dirksen M, Knap WH, Steeneveld G-J, Holtslag AAM, Tank AMGK. Downscaling daily air-temperature measurements in the Netherlands. Theor Appl Climatol 2020;142(1-2):751–67.
[35] Chongcong T, Chao Z, Hongli Ji, Jinhao Q. Fatigue life prediction of GFRP laminates using averaged Bayesian predictive distribution and Lamb wave velocity. Compos Sci Technol 2020;196:108213. https://doi.org/10.1016/j.compscitech.2020.108213.
[36] Grahn T. Lamb wave scattering from a circular partly through-thickness hole in a plate. Wave Motion 2003;37(1):63–80.
[37] Coble JB. Merging Data Sources to Predict Remaining Useful Life – An Automated Method to Identify Prognostic Parameters. PhD: University of Tennessee; 2010.
[38] Fendzi C, Rébillat M, Mechbal N, Guskov M, Coffignal G. A data-driven temperature compensation approach for Structural Health Monitoring using Lamb waves. Struct Health Monit 2016;15(5):525–40.